Time-of-flight scattering and recoiling spectrometry. II. The structure of oxygen on the W(211) surface

H. Bu, O. Grizzi,* M. Shi, and J. W. Rabalais
Department of Chemistry, University of Houston, Houston, Texas 77204-5641
(Received 14 April 1989)

The technique of time-of-flight scattering and recoiling spectrometry (TOF-SARS) with detection of both neutrals and ions is applied to structural analysis of oxygen adsorbed on a W(211) surface. The site position for oxygen in the high-dose [$\Theta=1.5$ monolayers (ML), saturation coverage] $p(1\times2)$ low energy electron diffraction (LEED) pattern is determined; a preliminary study of oxygen in the low-dose ($\Theta=0.5$ ML) $p(2\times1)$ LEED pattern is also presented. Both Ar and Ne backscattering (BS) and oxygen recoiling spectra, induced by pulsed 4-keV Ar^+ and 5-keV Ne^+ primary-ion beams, are monitored as a function of polar beam incident angle α, surface azimuthal angle δ, scattering angle θ, and recoiling angle ϕ. Plots of BS (or recoil) intensities in (α,δ) space provide scattering (or recoiling) structural contour maps and three-dimensional scattering (or recoiling) structural plots which are representative of the adsorption sites of oxygen on the W(211) surface; the symmetry of the adsorption sites is determined from these plots. Measurements of BS and recoil intensities as a function of α along different azimuths δ provide experimental values of the critical incident angles $\alpha^i_{c,\mathrm{sh}}$ for shadowing and the critical ejection angles β_c (or $\alpha_{c,\mathrm{bl}}$) for blocking by neighboring atoms. Trajectory simulations and calculations of the shadowing and blocking cones obtained from potentials calibrated for this system are used to determine the oxygen-adsorption-site coordinates. The results show that oxygen is dissociatively adsorbed within the troughs along the $[1\,\bar{1}\,\bar{1}]$ direction. For the saturation $p(1\times2)$ structure, the oxygen is in threefold sites formed by two first- and one second-layer W atoms; these are the only sites which are consistent with all of the experimental data. The coordinates of these sites relative to the W coordinates are determined to an accuracy of ±0.1 Å. The oxygen-tungsten chemisorption bond length is determined as 1.83 Å to the two first-layer W atoms and 2.17 Å to the second-layer W atom; this reflects the unsaturated and fully saturated valencies of the first- and second-layer W atoms, respectively. These trough sites are occupied for coverages up to more than one monolayer of oxygen. For the low-dose $p(2\times1)$ structure, the data indicate occupancy of the same threefold sites, but with different coordinates. The data are consistent with shifting of the relaxed clean W surface structure to the bulk truncated structure upon O_2 chemisorption. The sensitivity of TOF-SARS to details of adsorbate structure, the use of both BS and recoil data in a complementary manner, and the ability to extract adsorbate structural information with only simple calculations are presented.

I. INTRODUCTION

While there exists an impressive array of surface-science techniques[1] for elemental analysis of adsorbates on surfaces that can provide information on adsorption and desorption kinetics and thermodynamics, adsorbate electronic structure, and the symmetry of adsorbate sites, it is considerably more difficult to obtain direct "real-space" information on the precise coordinates of absorbate-site positions. The currently most widely used methods for studying adsorbate structures are low-energy electron diffraction (LEED), surface extended x-ray-absorption fine structure (SEXAFS), and scanning tunneling microscopy (STM). Although these techniques have made extensive, excellent contributions to the understanding of absorbate structures, there is need for a simple, direct adsorbate crystallographic technique. Ion-scattering[2] and -recoiling[3–5] spectrometry in the keV range directly samples atomic core positions and can provide "real-space" interatomic distances and adsorbate-site coordinates from shadowing- and blocking-cone analysis. Ion-scattering spectrometry itself has poor sensitivity to light adsorbates due to the low scattering cross sections and absence of backscattering from light atoms. However, measurements of these light adsorbates as recoiled atoms coupled with adsorbate perturbations on backscattered (BS) trajectories can provide a sensitive structural analysis.

This is the second (II) member of a series of three papers, I (Ref. 6) and III (Ref. 7), in which we describe and apply the technique of time-of-flight scattering and recoiling spectrometry (TOF-SARS) for determination of oxygen adsorbate structure and site coordinates. Details of the TOF-SARS technique are described in I,[6] where it is applied to determination of the relaxed structure of a clean W(211) surface. The purpose of this paper is two-fold: First, to demonstrate the ability of TOF-SARS to directly determine adsorbate site positions and site coordinates in real space with only simple computational procedures; second, to resolve the long-standing problem of the nature of the oxygen adsorption sites on the W(211) surface. Resolution of structure on an atomic scale is ob-

tained by collecting scattering and recoiling data as a function of the scattering angle θ, recoiling angle ϕ, incident angle α, ejection angle β, and azimuthal angle δ. The experimental data used in this analysis are TOF spectra of neutral plus ion Ar and Ne backscattering intensities $I(\mathrm{BS})$ at $\theta=163°$ and oxygen recoiling intensities $I(R)$, both direct (DR) and surface (SR) recoils, in the forward-scattering (FS) range $0° \leq \phi \leq 65°$. Scattering and recoiling structural contour maps (SSCM and RSCM) and three-dimensional scattering and recoiling structural plots (SSP and RSP) are presented for the saturation O_2 dose [$\Theta=1.5$ monolayer (ML)]. The computations employed are classical-trajectory simulations and shadowing- and blocking-cone analysis. A list of abbreviations and symbols is provided in I.[6]

Chemisorption of oxygen on W(211) surfaces has been studied by a host of surface-science techniques, including electron diffraction (both LEED and RHEED), Auger-electron spectroscopy (AES), x-ray photoelectron spectroscopy (XPS), thermal-desorption spectrometry (TDS), electron-energy-loss spectroscopy (EELS), and $^3He^+$ scattering.[8-17] There is general agreement that dissociative chemisorption of oxygen occurs at room temperature and is characterized by three distinct coverage-dependent LEED patterns: (a) $p(2\times1)$ pattern at half-monolayer coverage ($\Theta=0.5$ ML), a $p(1\times1)$ pattern at one-monolayer coverage ($\Theta=1.0$ ML), and a $p(1\times2)$ pattern at one-and-a-half–monolayer coverage ($\Theta=1.5$ ML). There is, however, disagreement concerning the assignment of the adsorption sites that correspond to these LEED patterns.

Part of the difficulty is due to the fact that there are several possible geometrically different absorption sites on W(211) surfaces as shown in Fig. 1. The surface consists of close-packed rows of atoms along the $[1\bar{1}\bar{1}]$ direction separated by wide channels or "troughs" in which the second atomic layer is displaced relative to the first atomic layer such that there is no plane of symmetry about the $[01\bar{1}]$ azimuth. In this paper the azimuths are labeled according to $\delta=0°$ along $[01\bar{1}]$, $\delta=-90°$ along $[1\bar{1}\bar{1}]$, and $\delta=+90°$ along $[\bar{1}11]$, and the angular notation for the beam direction is defined as shown in Fig. 1. The second-layer atoms are directly exposed in these troughs despite the fact that they have their full complement of nearest neighbors. There are two different adsorption site models predicted from LEED studies. *First model*:[11] Oxygen atoms are adsorbed within the troughs in threefold sites formed by the first- and second-layer W atoms [trough site (5) in Fig. 1] from low coverages up to more than one monolayer, i.e., as high as $\Theta=1.66$ ML. *Second model*:[14-16] At low coverages, $\Theta\leq1.0$ ML, oxygen atoms are adsorbed within the troughs in bridging sites between two second-layer W atoms [symmetrical trough sites such as site (4) in Fig. 1] while at higher coverages ($1.0<\Theta\leq1.5$ ML) adsorption occurs on top of the rows in bridging sites between two first-layer W atoms [symmetrical row sites such as site (2) in Fig. 1]. Recent $^3He^+$ scattering results[17] have identified the probable adsorption site in agreement with the first model; however they did not provide coordinates for the site. In this work we will consider all eight geometrically different sites in Fig. 1 and will show that the data are consistent with occupancy of only one of those sites.

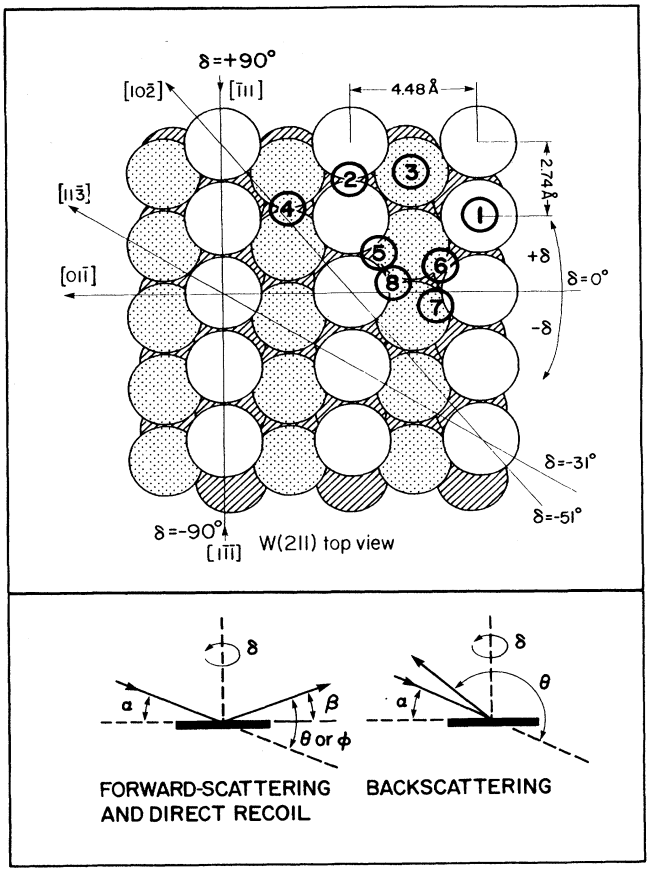

FIG. 1. Geometrically different adsorbate sites on the W(211) surface. The sizes of the atoms are scaled to the covalent radii of oxygen (adsorbate) and tungsten (substrate). Interatomic spacings for the bulk-truncated surface are indicated. The adsorption sites are defined as follows: on-top (1) and bridging (2) row sites, on-top (3) and bridging (4) trough sites, threefold trough sites (5), and asymmetrical (6–8) trough sites. The definition of angles used herein is indicated in the bottom drawing.

The organization of this paper is as follows. The experimental methods are briefly described in Sec. II. Section III presents the experimental data [TOF spectra, $I(\mathrm{BS})$ and $I(R)$ versus α and δ] and qualitative interpretations of the results. Section IV provides both a qualitative identification and quantitative analysis of the oxygen adsorption sites for the $p(1\times2)$ structure. The behavior of the data as a function of O_2 dose is considered in Sec. V. The discussion of Sec. VI relates the results to previous studies and describes the model for oxygen adsorption that can be derived based on this and previous work. Section VII provides the conclusions.

II. EXPERIMENTAL METHODS

A. TOF-SARS instrument, sample preparation, and spectral acquisition

The TOF-SARS spectrometer system and methods of orienting the sample, collecting data, and cleaning the W crystal are described in I.[6] The experimental parameters[18] used in these measurements were as follows: 4-keV Ar^+ and 5-keV Ne^+ pulsed primary-ion beams; ~50-ns pulse width, 0.50–1.0 nA/mm^2 average current density, ~20-sec spectral collection time, 98.4-cm flight path. The O_2 gas (Matheson 99.999%) was introduced through a variable leak valve; the dosing procedure was to heat the crystal up to 2300 K and then expose it to O_2 at a pressure of 1×10^{-8} Torr after the crystal had cooled down to ~200° C. Using such a procedure, the only adsorbate detectable on the surface by both AES and TOF-SARS was oxygen. Impurities such as carbon and hydrogen were not detected, even though TOF-SARS is capable of detecting such light adsorbates in quantities of <0.01 ML.[3] The oxygen coverage on the surface was determined from both AES and LEED measurements. AES intensities were determined from peak amplitudes in the derivative mode for the O(*KLL*) transition at 503 eV and the W(*MNN*) transition at 350 eV using a hemispherical electron analyzer mounted in the same spectrometer system. The I(O)/I(W) AES intensity ratios for each LEED pattern were in good agreement with those of Table I in Ref. 11. The clean surface produced a sharp (1×1) LEED pattern. A series of well-defined LEED patterns were observed as a function of O_2 exposure as determined previously.[11–16] Initial exposure resulted in a $p(2\times1)$ pattern, slightly higher exposure produced a $p(1\times1)$ pattern, and continued exposure produced a $p(1\times2)$ pattern. In collecting I(BS) and $I(R)$ versus incident angle α scans, the sample was cleaned by annealing to 2300 K and redosing with O_2 following every α scan. The surface cleaniless was checked by TOF-SARS and/or AES after annealing in order to ensure that the surface was clean before redosing with O_2. Structural analyses were performed on both the $p(2\times1)$ and $p(1\times2)$ LEED patterns but not on the intermediate $p(1\times1)$ pattern.

B. General procedure for adsorbate structural determination

The general procedure for adsorbate structural determination by TOF-SARS is as follows. (i) I(BS) versus incident angle α scans are measured along various azimuths for the adsorbate covered surface and compared to those for the clean surface. Differences indicate those azimuths along which the ion trajectories are perturbed by the adsorbate, providing a qualitative identification of the adsorbate sites. (ii) The surface structure is studied in order to determine the possible geometrically different adsorption sites that are consistent with the data of (i). (iii) $I(R)$ versus α scans are made along those azimuths where the adsorbate site is both visible to the beam and aligned with neighboring lattice atoms. (iv) These data, along with the shadowing and blocking cones, are used to select the adsorption site that is consistent with all of the results and to eliminate other sites. (v) The adsorption site coordinates relative to the substrate lattice are determined from the $I(R)$ versus α data and the calibrated cones. Rather than follow this procedure, this paper provides considerable detail on spectral interpretation, spectral sensitivity to lattice features, scattering and recoiling trajectories, and symmetry features of the scattering and recoiling data. The objective of this is to familiarize the reader with the rich information content of the scattering and recoiling data.

III. EXPERIMENTAL RESULTS AND INTERPRETATIONS

This section presents the experimental results in the form of example TOF sepctra and scans of I(BS) and $I(R)$ as a function of polar incident angle α and azimuthal angle δ along with their qualitative interpretations. Examples of the TOF spectra are provided in Sec. III A. The results for the saturation coverage $p(1\times2)$-O pattern are presented first and in considerable detail; I(BS) versus α and δ along with the SSCM and SSP are presented in Sec. III B and $I(R)$ versus α and δ along with the RSCM and RSP are presented in Sec. III C. The results for the low-coverage $p(2\times1)$-O pattern are presented in Sec. III D.

A. TOF spectra

The structural analyses made herein require the intensities of the BS and recoil peaks from the TOF spectra. Examples of BS and FS TOF spectra for 4-keV Ar^+ scattering from the W(211)-$p(1\times2)$-O surface are shown in Fig. 2. The scattered and recoiled atoms can be distinguished from each other by means of their TOF. For an incident ion of mass M_1 and energy E_0, the TOF of the ion after (quasi)single scattering (SS) from a target atom of mass M_2 is given in I (Ref. 6) and the TOF of the target atom *DR* into an angle ϕ is

$$t_{DR}=l(M_1+M_2)/(8M_1E_0)^{1/2}\cos\phi\ , \tag{1}$$

where l is the distance from the target to the detector. For $M_2/M_1<1$, large-angle BS cannot occur for heavy projectiles (Ne^+, Ar^+) hitting light atoms (H,C,O) since the maximum single-collision scattering angle is $\theta_c=\sin^{-1}M_2/M_1$.

1. Scattering peaks

The positions of the sharp scattering peaks in both the BS and FS TOF spectra were independent (within 0.1 μsec) of the α and δ orientations, confirming that the major contribution to these peak intensities is from SS collisions,[6] as for the clean surface. Since the maximum scattering angle[2,3] for Ar^+/O collisions is 23.6°, the only type of SS possible at the BS ($\theta=163°$) and FS ($\theta=65°$) angles employed is Ar SS from W atoms. Multiple scattering (MS) sequences are responsible for the shoulder on the short TOF side of the FS-SS peak and the

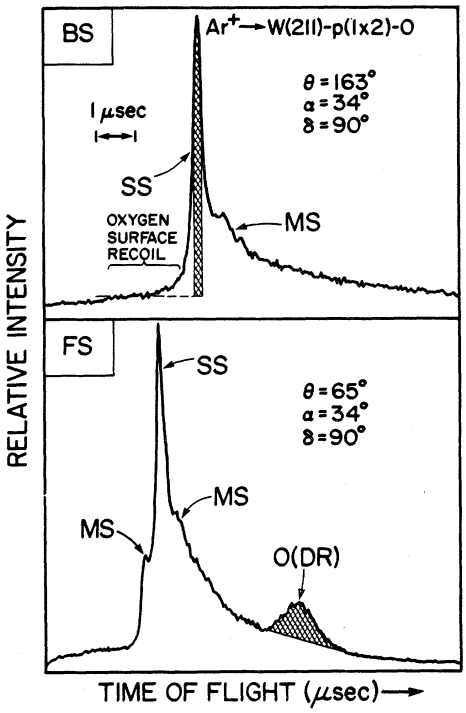

FIG. 2. Examples of backscattering (BS) and forward-scattering (FS) TOF spectra for 4-keV Ar^+ scattering from a W(211)-$p(1\times2)$-O surface. The beam direction was along the $[\bar{1}11]$ azimuth, the BS spectrum was collected at $\theta=163°$, $\alpha=34°$, and the FS spectrum was collected at $\theta=65°$, $\alpha=34°$. The areas measured as representative of Ar(BS) intensity I(BS) and O(DR) intensity I(DR) are shown hatched. Single-scattering (SS), multiple-scattering (MS), direct-recoil (DR), and surface-recoil (SR) structures are indicated.

broadening on the long TOF side of both the FS- and BS-SS peaks. Only the BS spectra were used for structural determinations because (i) the BS trajectories are simpler than the FS trajectories and (ii) the BS peaks are dominated by SS collisions while the FS peaks contain both SS and MS collisions. Very-low-intensity surface recoil[3] structure occurs on the short TOF side of the BS-SS peak but is too weak to be observed in Fig. 2. SR is due to O atoms that are recoiled from AR into a FS angle and then scattered from the W lattice.[3] The intensities of the BS-SS peaks, I(BS), were used in the adsorbate structure determinations. The widths of these BS peaks were 0.3 ± 0.1 μsec FWHM. As a representative measure of I(BS), the counts were integrated over a TOF window of 0.4 μsec centered over the SS peak maximum following background subtraction. The background was taken as the average number of counts/channel on the short TOF side of the BS peak multiplied by the number of channels in the TOF window, as shown in Fig. 2. Using this procedure, the error in determining the I(BS) peak areas was $<10\%$.

2. Recoiling peaks

The FS spectrum of Fig. 2 exhibits a typical example of an oxygen recoil peak that was used in the adsorbate structure determinations. As a representative measure of the intensity, $I(R)$ of these peaks, the counts were integrated over an area defined by drawing a straight line from the background on the short TOF side of the recoil peak to the background on the long TOF side as shown in Fig. 2. If small recoil angles are used, e.g., $\phi<45°$, the recoil peak is on the short TOF side of the scattering peak. At the recoiling angle employed, $\phi=65°$, the recoil peak is on the long TOF side of the scattering peak; this shift in the position of the recoil peak is due to the $(\cos\phi)^{-1}$ dependence [Eq. (2)] of the TOF for the DR species. The large-ϕ case was used herein for the following reasons. First, for small ϕ the recoil peak was sometimes partially overlapped by the MS shoulder, requiring deconvolution for quantifying. Second, for large ϕ the position of the recoil peak is extremely sensitive to the exact recoiling sequence, i.e., DR and SR events are well separated at large ϕ. Third, O atoms in subsurface layers cannot be sampled at low ϕ due to shadowing and blocking. The error in measuring the $I(R)$ peak areas was $<20\%$ for $\alpha\gtrsim20°$ where the data for quantitative analyses were acquired. Larger errors occurred for very low α; however these measurements were not used in the quantitative analyses. Since the variations in $I(R)$ as a function of α and δ were greater than a factor of 2, the $<20\%$ errors in the quantitative measurements were tolerable.

3. Dependence of recoil peaks on incident angle α and oxygen coverage Θ

A series of FS spectra along the $[10\bar{2}]$, $\delta=-51°$ azimuth is shown in Fig. 3 in order to illustrate the strong dependence of the recoil peak position on α. At $\alpha=10°$ the recoil structure splits into two peaks, with one peak drifting towards lower TOF as α increases until it underlies the Ar scattering peak and, in some cases, it even moves to the low TOF side of the scattering peak; this is a result of a SR sequence. The light O atom can FS from W with very little energy loss, while the energy of DR has a $\cos^2\phi$ dependence on the recoil angle ϕ For $\alpha<\approx15°$, specific sequences such as low-angle O recoil (ϕ near 0°) followed by O scattering from W (θ near 65°) can produce O which is significantly faster than that produced from a single-collision DR event with $\phi=65°$. $I(R)$ for such cases was obtained by drawing background lines, as described above, for both DR and SR peaks and summing the areas. The peak identified as DR shifts by ~0.6 μsec between $\alpha=10°$ and 12° and then remains constant up to high-α values. The shorter TOF at low α is due to sequences in which $\phi<65°$ and the recoiled O is deflected by W into 65°. For example, a 0.6-μsec shift from a true 65° recoil can be obtained by O recoiling at $\phi=63.4°$ and then being deflected from W at $\theta=1.6°$. Only data for $\alpha>12°$ were used in the quantitative determinations.

The sensitivity of the FS spectra along the $[11\bar{3}]$ azimuth to different oxygen coverages, i.e., low coverage ($\Theta<0.5ML$) and the $p(1\times2)$ high coverage ($\Theta=1.5$ ML) structures, is shown in Fig. 4. For the $p(1\times2)$ structure the spectrum is dominated by two intense recoil peaks which overshadow the Ar SS peak. For the low-

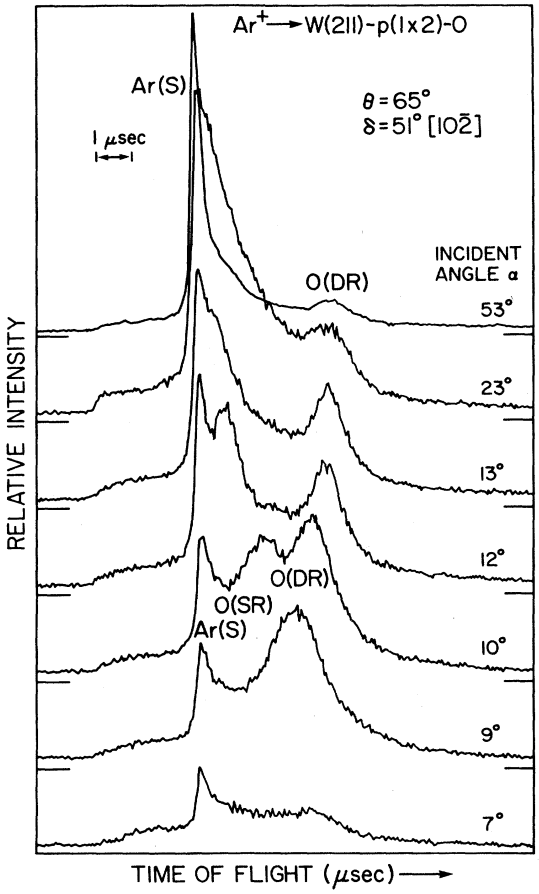

FIG. 3. Series of FS spectra along the [10$\bar{2}$] azimuth with $\theta=65°$ and several different α values. Splitting of the recoil peak into DR and SR components in the region $\alpha=10°-12°$ is observed.

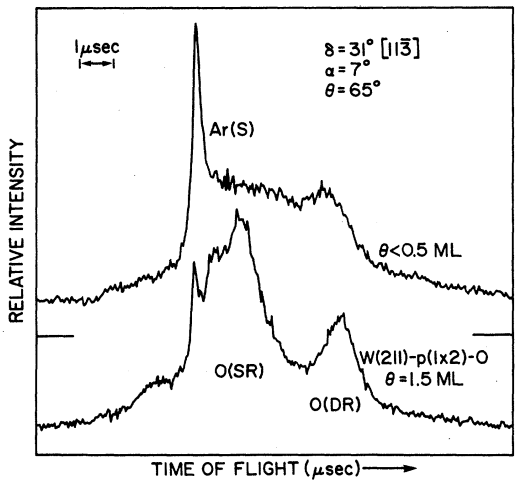

FIG. 4. Examples of FS spectra along the [11$\bar{3}$] azimuth for low ($\Theta<0.5$ ML) and high ($\Theta=1.5$ ML) oxygen coverages.

coverage structure the low TOF recoil peak is greatly reduced and the high TOF recoil peak remains clearly visible. Two peaked recoil structures are observable only for high oxygen coverage at low α along all azimuths *except* $\delta=\pm90°$. The lower TOF recoil peak for $p(1\times2)$ is due to SR sequences as described above.

B. Backscattering intensity I(BS) versus polar incident α and azimuthal δ angles for the $p(1\times2)$-O structure

1. *I(BS) versus α*

Collecting I(BS) data as a function of α for the oxygen covered surface and comparing this data to that of the clean surface allows one to qualitatively locate the oxygen site positions. Example plots of experimental BS Ar intensities $I(\mathrm{BS})\sin\alpha$ at $\theta=163°$ versus incident angle α are shown in Fig. 5 for four different crystal azimuths δ for the clean and $p(1\times2)$-O surface conditions. The $\sin\alpha$ correction[6] accounts for the variation in the sampling area as a function of α. These plots exhibit a low-α peak, $\alpha^1_{c,\mathrm{sh}}$ followed by one, $\alpha^2_{c,\mathrm{sh}}$, or more, $\alpha^i_{c,\mathrm{sh}}$, intense high-α peaks. In general, the $\alpha^1_{c,\mathrm{sh}}$ peak corresponds to BS from the first-atomic layer and the $\alpha^i_{c,\mathrm{sh}}$ $(i>1)$ peaks correspond to BS from second-(and sometimes deeper) atomic layers.[6] For the W(211) surface this is modified along the $\delta=\pm90°$ azimuths where the second-layer W atoms are directly exposed to the beam; here $\alpha^1_{c,\mathrm{sh}}$ corresponds to both first- and second-layer scattering and $\alpha^2_{c,\mathrm{sh}}$ corresponds to third- and fourth-layer scattering. The critical incident angle $\alpha_{c,\mathrm{sh}}$ positions of the sharp rises in I(BS) versus α, measured at one-half of the peak height minus the background, are very similar along some azimuths

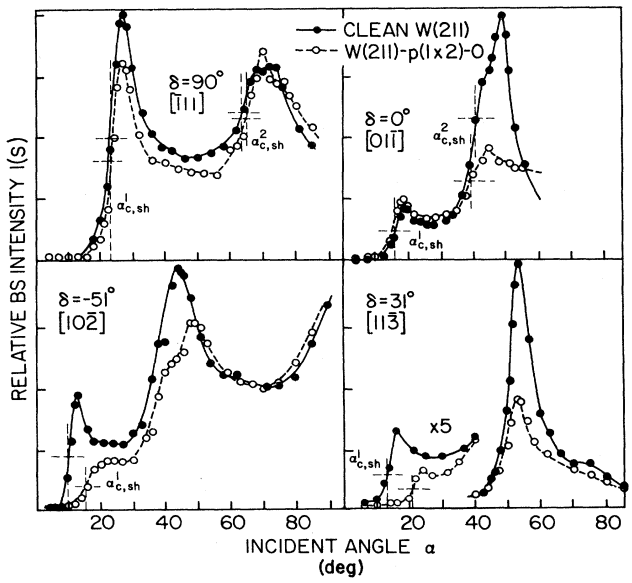

FIG. 5. Examples of experimental BS Ar neutral plus ion $(N+I)$ intensities I(BS) as a function of incident angle α at $\theta=163°$ for several different crystal azimuths δ of the clean and $p(1\times2)$-O surfaces. The $\alpha^i_{c,\mathrm{sh}}$ values are indicated. Lines are used to connect the data points in order to guide the eye.

and different along others when the clean and $p(1\times2)$-O scans are compared. For example, the $\alpha^1_{c,sh}$ and corresponding I(BS) for $\delta=0°$ and 90° are insensitive to the presence of oxygen, while for $\delta=31°$ and $-51°$ the presence of oxygen results in a $\sim7°$ increase in $\alpha^1_{c,sh}$ and conversion of the peaked structure to a stepped structure. For the $\alpha^2_{c,sh}$ peaks,, some exhibit total insensitivity to oxygen ($\delta=90°$) while others are attenuated by oxygen. Structures which are totally insensitive to the oxygen are those for which the Ar trajectories are unperturbed by the presence of oxygen, i.e., the oxygen is not in the path of the scattering Ar. Structures which are sensitive to oxygen are those for which the oxygen atoms lie along or very near the path of the scattering Ar. Although Ar cannot backscatter from O, the presence of O atoms near the scattering trajectory results in small-angle deflections of the Ar which are sufficient to produce the changes observed in Fig. 5.

2. *Scattering structural contour map and scattering structural plot*

I(BS) as a function of α along different crystal azimuths for $-90°\leq\delta\leq+90°$ are shown as a scattering structural contour map and a three-dimensional scattering structural plot in Figs. 6 and 7, respectively, for the $p(1\times2)$-O surface. The scans were taken at increments of $\alpha=1°$, 2°, or 3° and $\delta=6°$ and an interpolation routine was used between the points from adjacent α scans along each δ. The critical value of α at low angles, $\alpha^1_{c,sh}$, is also plotted in Fig. 6. The SSCM and SSP provide the following information. (i) They are a concise summary of the experimental BS data. (ii) They reveal any adsorbate-induced surface reconstruction by comparison to the clean surface pattern. (iii) They show what general regions of (α,δ) space are different from the clean surface plots, thereby revealing the positions of the adsorbates for further, more detailed investigation. Consider the general features of the SSCM and SSP. By comparison to the SSCM and SSP for clean W(211) [see Figs. 6 and 7 of I (Ref. 6)], it is observed that the patterns are preserved when oxygen is adsorbed. Since the symmetry of these patterns is determined by the W structure, i.e., BS results entirely from W atoms, this preservation of the symmetry indicates that oxygen adsorption *does not* reconstruct the basic symmetry of the clean W(211) surface. However, small differences in these SSCM's and SSP's occur throughout (α,δ) space as follows. All of the peaks due to shadowing of second-layer atoms by their first-layer neighbors are shifted to 3°–4° higher α values upon O_2 chemisorption. Other critical differences occur at low α where low-intensity structures due to shadowing of first-layer atoms by their first-layer neighbors occur. Since the plots of Figs. 6 and 7 are normalized to the intense structure at $\alpha=53°$, $\delta=42°$, these low-intensity features are obscured. In order to emphasize these differences, SSCM's are plotted for the clean and $p(1\times2)$-O surfaces in Fig. 8 for the range $0°\leq\alpha\leq40°$. Large differences occur at low α along

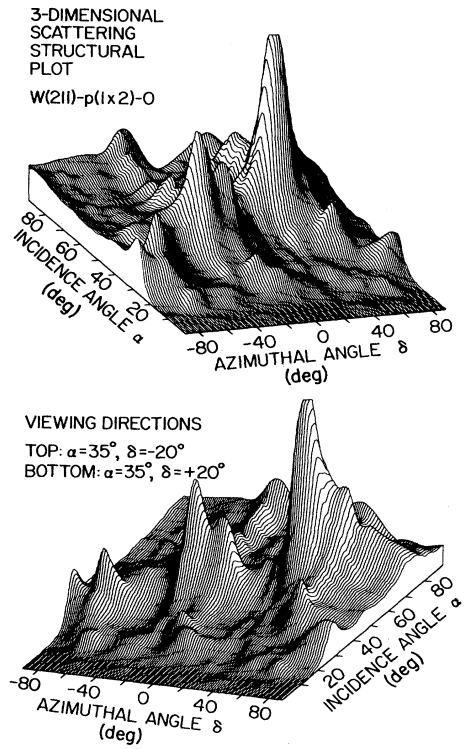

FIG. 7. Three-dimensional scattering structural plot (SSP) for the W(211)-$p(1\times2)$-O surface. Viewing directions are $\alpha=35°$, $\delta=-20°$ (top) and $\alpha=35°$, $\delta=20°$ (bottom). Azimuths are defined as in Fig. 6.

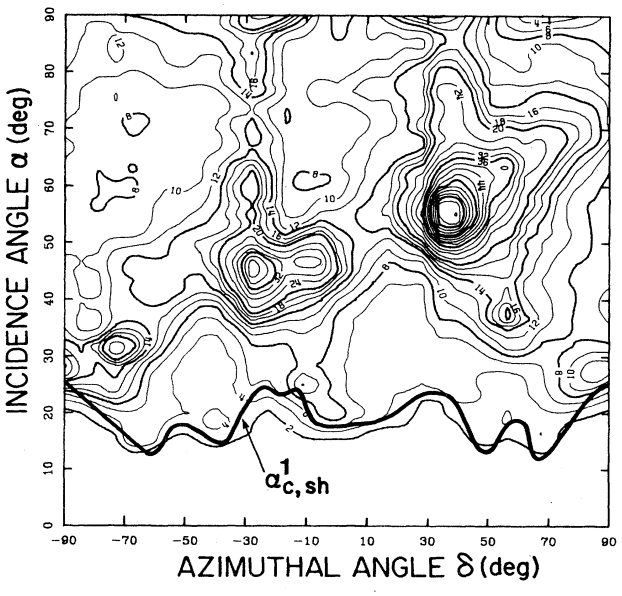

FIG. 6. Scattering structural contour map (SSCM) for the W(211)-$p(1\times2)$-O surface for $0°\leq\alpha\leq90°$. Primary ion: 4-keV Ar^+; $\theta=163°$; $\delta=0°$ is the $[01\bar{1}]$ azimuth; $\delta=-90°$ is the $[1\bar{1}\bar{1}]$ azimuth; $\delta=+90°$ is the $[1\bar{1}\bar{1}]$ azimuth. The critical value of α at low angles, $\alpha^1_{c,sh}$, is plotted on the map.

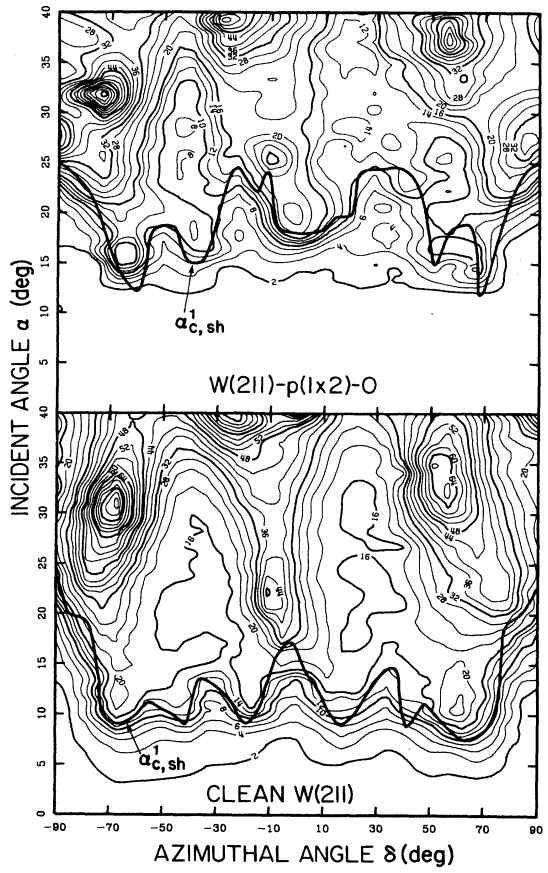

FIG. 8. Scattering structural contour maps (SSCM) for the W(211)-$p(1\times2)$-O surface (top) and the clean W(211) surface (bottom) for $0°\leq\alpha\leq40°$. Azimuths are defined in Fig. 6. The critical value of α at low angles, $\alpha^1_{c,sh}$, is plotted on the map.

certain δ. For $\delta=0°$ and $\pm90°$, the low-α maxima occur near 19° ($\alpha^1_{c,sh}=16.1°$) and 27° ($\alpha^1_{c,sh}=23.2°$), respectively, for both cases. Along intermediate azimuths the first maxima for the $p(1\times2)$-O surface are at considerably higher (sometimes 5°–6° higher) α values than those of the clean surface.

C. Recoil intensity $I(R)$ versus polar incident α and azimuthal δ angles for the $p(1\times2)$-O structure

1. I(R) versus α

Collecting $I(R)$ data as a function of α allows one to probe the ability of (i) the incident ions to hit the oxygen sites, i.e., the entrance channel, and (ii) the recoiling oxygen to escape from the surface, i.e., the exit channel. Example plots of experimental oxygen recoil intensities $I(R)$ at $\phi=65°$ versus incident angle α are shown in Fig. 9 for seven different crystal azimuths, chosen as three $\pm\delta$ positions and $\delta=0°$, for the W(211)-$p(1\times2)$-O surface. The $I(R)$ exhibit sharp structural features as a function of α; the structures observed indicate that O atoms in different positions are accessible at different α. First, the

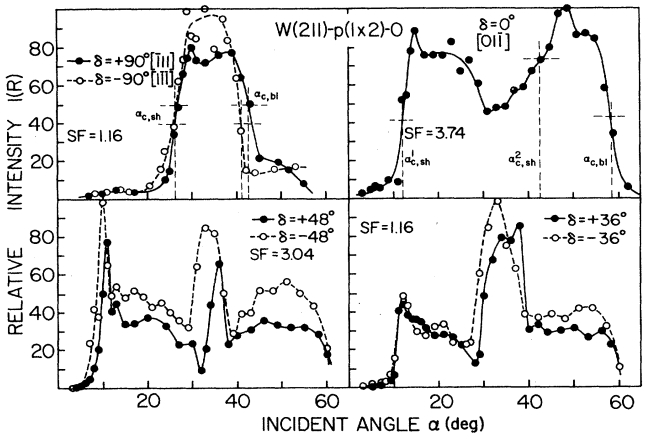

FIG. 9. Examples of experimental recoil oxygen neutral plus ion ($N+I$) intensities as a function of incident angle α at $\phi=65°$ for several different azimuths δ of the W(211)-$p(1\times2)$-O surface. Lines are used to connect the data points in order to guide the eye. The scaling factors (SF) indicate the numbers by which the spectral points were multiplied in order to place the peak of maximum intensity at full scale. The $\alpha^i_{c,sh}$ and $\alpha_{c,bl}$ values are indicated for the $\delta=0°$ and $\pm90°$ azimuths.

sharp *increases in I(R)* are determined by shadowing cones of Ar scattering from W and O that focus the projectiles and restrict Ar/O collisions of the appropriate p for O(R) into 65°. These are similar to the I(BS) features of Fig. 5, with the exception that an Ar/O DR collision into 65° requires a significant p (0.355 Å) while the p for an Ar/W BS collision into 163° is small (0.037 Å). Note that Ar can scatter from O for large-p collisions where $\theta<23.5°$. Some of the scans exhibit two sharp increases in $I(R)$, defining the two critical values $\alpha^1_{c,sh}$ and $\alpha^2_{c,sh}$, respectively; these α_c's are determined as one-half the peak height minus the background as in I.[6] Second, the sharp *decreases* in $I(R)$ at high α are determined by neighboring W and O blocking cones which restrict O recoils. The critical value of this structure, $\alpha_{c,bl}$, is also determined as one-half the peak height minus the background. Two peaked (or more) structures, which drop off sharply near $\alpha=58°$, are observed along all δ, with the exception of the $\delta=\pm90°$ azimuths. For $\alpha_{c,bl}=58°$, the ejection angle $\beta_c=7°$; this defines the critical ejection angle $\alpha_{c,bl}$ (or β_c) for blocking of O(R) by neighboring W atom blocking cones and, thus, the size of the blocking cones. Along the $\delta=\pm90°$ azimuths a rather sharp structure is observed which begins at higher α and ends at lower α than along the other azimuths; here the $\alpha_{c,sh}$ and $\alpha_{c,bl}$ values are determined by O atoms shadowing and blocking neighboring O atoms.

The $I(R)$ structures of Fig. 9 and the $\alpha^{1,2}_{c,sh}$ and $\alpha_{c,bl}$ values along $\pm\delta$ azimuths are similar, illustrating the symmetry of the adsorption sites about the $\delta=0°$ direction. Along the $\delta=\pm48°$ azimuths, the $\alpha^2_{c,sh}$ values (near $\alpha=33°$) differ by $\sim4°$. This discrepancy is attributed to the poor counting statistics due to the low $I(R)$ (note the large SF value) along this azimuth and an uncertainty in δ at the time of one of the measurements.

2. $I(R)$ versus δ

Collecting $I(R)$ data as a function of δ allows determination of the azimuths along which the O(R) channel is accessible or obstructed. For this purpose the second I(DR) peak of Fig. 9, i.e., $\alpha^2_{c,\mathrm{sh}}$, is used since the interfering SR events are minimized at this high-α position. From the scaling factors (SF) in Fig. 9, it is observed that this second I(DR) structure exhibits large-intensity variations along the different azimuths. The I(DR) for this second peak is plotted as a function of δ in Fig. 10. The curves exhibit maxima at $\delta=\pm30°$ and $\pm90°$ and minima at $\delta=0°$ and $\pm54°$. These maxima and minima define the azimuths along which O(DR) is readily accessible and severely obstructed, respectively. These strong variations in I(DR) in the intermediate region $\delta=\pm(10°-80°)$ are due to W atoms shadowing O atoms rather than O atoms shadowing O atoms. This is determined as follows. The O-O distance (as will be shown later) is shorter along the direction $\delta=\pm90°$, where I(DR) is maximum, than along the direction $\delta=\pm54°$, where I(DR) is minimum. (Note that the $\alpha^2_{c,\mathrm{sh}}$ values in the bottom of Fig. 10 are similar along these azimuths.) If the variations in I(DR) were due to O-O interferences, these structures would be either two minima or would be reversed. Also, $\alpha\simeq30°$ [corresponding to the second $I(DR)$ peak] is above the O-O shadowing angle. Oxygen self-shadowing is primarily observed along $\delta=0°$ and $\pm90°$.

Also shown in Fig. 10 is a plot of $\alpha^2_{c,\mathrm{sh}}$ versus δ (this is the *only* α_c value in the case of $\delta=\pm90°$). It is observed that the maxima and minima in $\alpha^2_{c,\mathrm{sh}}$ occur at $\delta=0°$, $\pm51°$, and $\pm90°$ and $\delta=\pm18°$ and $\pm72°$, respectively. The maxima and minima in I(DR) mirror those of $\alpha^2_{c,\mathrm{sh}}$ at $\delta=0°$ and $\pm(51°-54°)$. The high $\alpha^2_{c,\mathrm{sh}}$ values indicate close-packed directions where O(DR) is hindered, resulting in low-I(DR) values. An exception to this is $\delta=\pm90°$, which exhibit maxima in both plots.

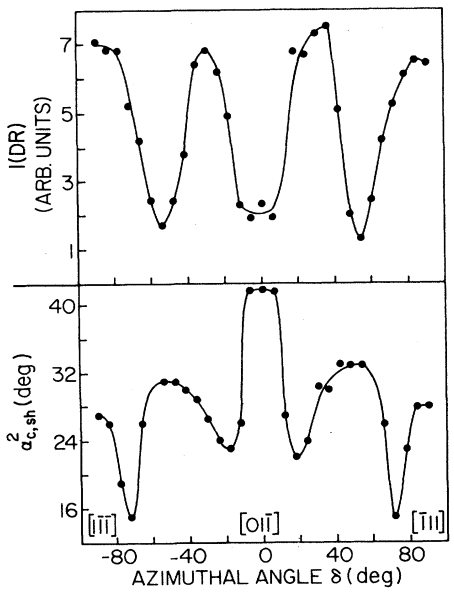

FIG. 10. Upper plot: I(DR) corresponding to the second peak, i.e., $\alpha^2_{c,\mathrm{sh}}$, in Fig. 9 as a function of azimuthal angle δ. Lower plot: $\alpha^2_{c,\mathrm{sh}}$ vs azimuthal angle δ.

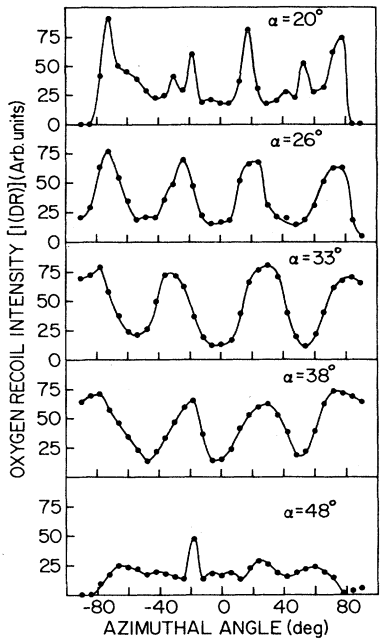

FIG. 11. Plots of oxygen recoil intensity $I(R)$ as a function of azimuthal angle δ for five different incident angles α on the W(211)-p(1×2)-O surface.

Plots of $I(R)$ at $\phi=65°$ as a function of azimuthal angle δ for different α values are shown in Fig. 11. The structure in $I(R)$ versus δ is symmetrical about the [01$\bar{1}$] ($\delta=0°$) azimuth for all $\alpha<\approx40°$. This data also shows that in the region $+85°>\delta>-85$, W atoms are shadowing O atoms rather than O atoms shadowing O atoms for the following reasons. First, the constant positions of the minima and maxima for $\alpha=26°$, 33°, and 38° in the region $+85°>\delta>-85°$ are indicative of the same type of shadowing in this region. Second, similar minima are observed at $\alpha=26°$ for $\delta=\pm90°$ and $\pm54°$ where the O-O interatomic distances are 2.74 and 3.51 Å, respectively; if O atoms would be shadowing O atoms, a significantly higher $I(R)$ would be expected at $\delta=\pm54°$ due to the longer interatomic distance. The change in $I(R)$ at $\delta=\pm90°$ from a minimum for $\alpha<30°$ to a maximum for $\alpha>30°$ indicates that the shadowing along these azimuths is different from the others, i.e., O atoms are shadowing O atoms in this case. For $\alpha\gtrsim40°$, $I(R)$ is low because there is no strong focusing at high α. Along $\delta=\pm90°$, the intensity is very low for $\alpha>40°$ due to strong blocking effects. A sharp focusing structure is observed at $\alpha=48°$ and $\delta=20°$.

3. *Recoiling structural contour map and recoiling structural plot*

The features of $I(R)$ in (α,δ)-space are shown in the form of a recoiling structural contour map and three-

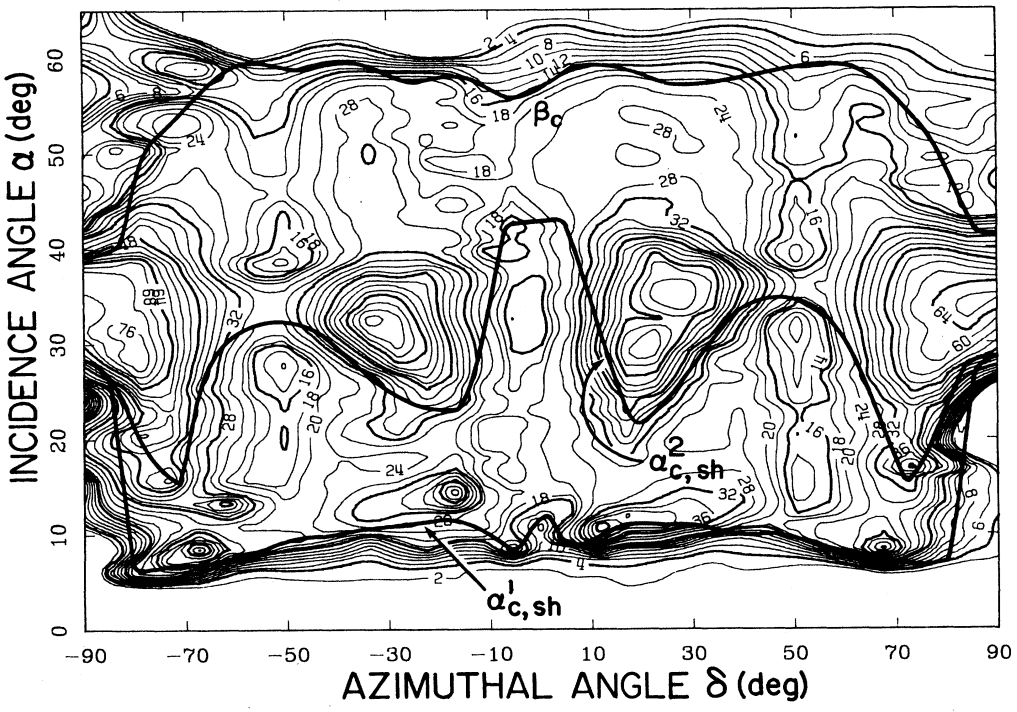

FIG. 12. Recoiling structural contour map (RSCM) for the W(211)-$p(1\times2)$-O surface. Azimuths are defined as in Fig. 6. The two critical shadowing angles $\alpha^1_{c,\mathrm{sh}}$ and $\alpha^2_{c,\mathrm{sh}}$ and the critical blocking angle β_c are plotted on the map.

dimensional recoiling structural plot in Figs. 12 and 13, respectively. The two critical shadowing angles $\alpha^1_{c,\mathrm{sh}}$ and $\alpha^2_{c\mathrm{sh}}$ and the critical blocking angle β_c are plotted in Fig. 12. The RSCM and RSP provide the following information. (i) They are a concise summary of the experimental $O(R)$ data. (ii) They reveal the symmetry of the $O(R)$ data in (α,δ) space, providing characteristic identification "*fingerprints*" for a specific adsorbate and coverage on a specific crystal face. Note that the features are symmetrical about the $[01\bar{1}]$ ($\delta=0°$) azimuth. Since the symmetry of the RSCM and RSP features is determined by the oxygen-site positions, this indicates that the adsorption sites are symmetrical about this direction. (iii) Changes in $\alpha^i_{c,\mathrm{sh}}$ and $\alpha_{c,\mathrm{bl}}$ reveal azimuths along which the shadowing and blocking conditions for $O(R)$ differ. The $\alpha^i_{c,\mathrm{sh}}$ corresponds to shadowing of O atoms by neighboring atoms (O or W) and the $\alpha_{c,\mathrm{bl}}$ corresponds to blocking of O recoil by neighboring atoms (O or W). The $\alpha^1_{c,\mathrm{sh}}$ value for $O(R)$ is relatively constant in the range $-80°<\delta<+80°$ and rises sharply for $|\delta|>85°$. Similarly, the $\alpha_{c,\mathrm{bl}}$ for $O(R)$, and consequently the minimum β value (β_c), is relatively constant at $\alpha_{c,\mathrm{bl}}\approx60°$, $\beta_c\approx5°$ in the range $-70°<\delta<+70°$; for $\delta>70°$ and $\delta<-70°$, the $\alpha^i_{c,\mathrm{sh}}$'s increase and $\alpha_{c,\mathrm{bl}}$'s decrease (β_c's increase) sharply to the values at the $\delta=\pm90°$ azimuths. This clearly points to a different type of shadowing and blocking along the $\delta=\pm90°$ azimuths. The extremely sharp structures for $\alpha<15°$ that are particularly prominent in the RSP are due to SR processes that appear in the low-α region.

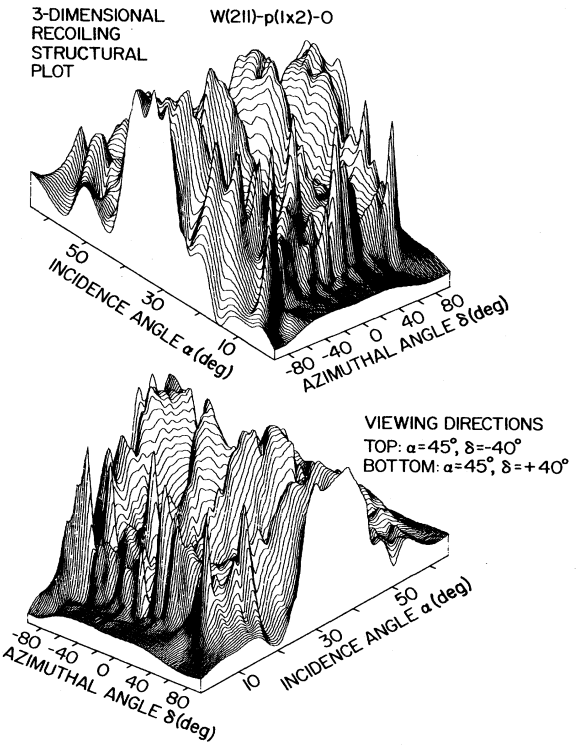

FIG. 13. Recoiling structural plot (RSP) for the W(211)-$p(1\times2)$-O surface. Viewing directions are $\alpha=45°$, $\delta=-40°$ (top) and $\alpha=45°$, $\delta=+40°$ (bottom) and azimuths are defined in Fig. 6.

D. Recoil intensity $I(R)$ as a function of incident angle α for different oxygen coverages

The $I(R)$ data as a function of α for different oxygen coverages allow determination of (i) different adsorption sites that are occupied as a function of coverage and (ii) the azimuths along which the O atoms become close packed as coverage increases. Plots of $I(R)$ versus α are shown in Fig. 14 for oxygen coverages corresponding to the low-dose $p(2\times1)$ structure and the saturation dose $p(1\times2)$ structure. Along both of the $\delta=\pm90°$ azimuths, $\alpha_{c,\mathrm{sh}}=24°$ and $\alpha_{c,\mathrm{bl}}=42°$ at high coverage, which is considerably higher and lower, respectively, than the values $\alpha_{c,\mathrm{sh}}=16°$ and $\alpha_{c,\mathrm{bl}}=48°$ obtained at low coverage. Along other azimuths, such as $\delta=31°$, the $\alpha^1_{c,\mathrm{sh}}$ and $\alpha_{c,\mathrm{bl}}$ values are nearly identical for different coverages. These data indicate that as coverage increases, both the shadowing and blocking effects become more severe along the $\delta=\pm90°$ azimuths than along other azimuths; this results from shadowing and blocking of O atoms by O atoms. It is also noted that along the $\delta=31°$ azimuth a second peak and corresponding sharp $\alpha^2_{c,\mathrm{sh}}$ value are observed only at high coverage. This appearance of a second peak at high coverage indicates that an additional adsorption site is being occupied which was previously unoccupied. The intensity of this second peak and its sharp onset is a result of focusing of Ar^+ trajectories by W atoms onto O atoms. This peak cannot be due to focusing of Ar^+ trajectories by O atoms onto O atoms because it occurs well above the $\alpha_{c,\mathrm{sh}}$ value for O atoms shadowing O atoms. Preliminary I(BS) and $I(R)$ versus α and δ scans have been acquired for the low-dose $p(2\times1)$-O structure. These data are also symmetrical about the $[01\bar{1}]$ azimuth.

IV. DETERMINATION OF THE SATURATION DOSE $p(1\times2)$ OXYGEN-ADSORPTION-SITE POSITIONS

The $p(1\times2)$ oxygen-adsorption-site position is determined in this section, beginnning with qualitative location of the position followed by quantitative analysis of the site coordinates relative to the W(211) structure. Several different methods are used for determination of the site coordinates and the results of each method are presented. Finally these results are collected and summarized.

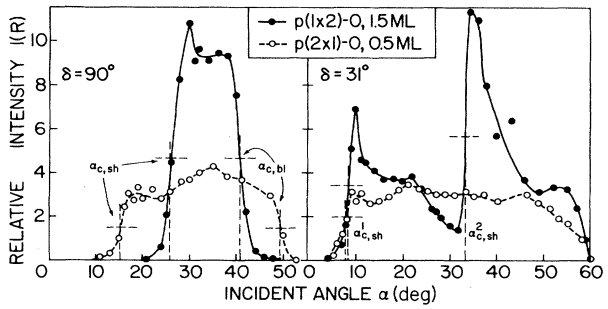

FIG. 14. $I(R)$ vs incident angle α plots for the high-coverage ($\Theta=1.5$ ML) $p(1\times2)$-O structure and the low-coverage ($\Theta=0.5$ ML) $p(2\times1)$-O structure at $\delta=31°$ and 90°. The $\alpha^i_{c,\mathrm{sh}}$ and $\alpha_{c,\mathrm{bl}}$ positions are indicated.

A. Qualitative identification of the site

A qualitative identification of the oxygen adsorption site position(s) from the eight geometrically different sites identified on the W(211) surface in Fig. 1 can be obtained from the data presented in Sec. III along with simple calculations. Summarized in Table III are the calculated positions for the strongest minima $\delta_{\min}$ in $I(R)$ versus δ scans for shadowing of oxygen atoms by neighboring tungsten atoms assuming that the oxygen resides in each of the eight sites in Fig. 1. These $\delta_{\min}$ represent the azimuths along which the O atom and first-layer W atoms are aligned for each site. The experimental minima corresponding to W shadowing O are those observed at $\pm(51°-54°)$ in Fig. 10 and the $\alpha=26°$, 33°, and 48° scans of Fig. 11. It will be shown that the experimental data are consistent with only dissociative chemisorption in the threefold trough sites labeled (5) in Fig. 1.

On-top row site (1). The presence of oxygen in these positions would interfere with BS trajectories along the $\delta=0°$ and $\delta=\pm90°$ azimuths for first-layer scattering, since such trajectories require $p\approx0°$ Ar^+/W collisions with no deflections. As observed in the I(BS) versus α plots of Fig. 5 and the SSCM's of Fig. 8, the $\alpha^1_{c,\mathrm{sh}}$ values for $\delta=0°$ and $\pm90°$ are within 1° and I(BS) is changed by $<20\%$ when the clean and $p(1\times2)$-O surfaces are compared. The minima in the $I(R)$ versus δ plots of Figs. 10 and 11 and the maximum in the $\alpha^2_{c,\mathrm{sh}}$ versus δ plot of Fig. 10 for $\delta=0°$ are also inconsistent with this site. In the latter case the interatomic oxygen distance would be long, facilitating (rather than hindering) high I(DR) and

TABLE I. Calculated positions of the strong minima in $I(R)$ vs δ scans for shadowing of oxygen by tungsten

Adsorption site (see Fig. 1)	Calculated $\delta_{\min}$ positions[a]
1	0°, ±31°, ±90°
2	±17°
3	+39°, −22°
4	+12°, −46°
5	±51°
6	+58°, −39°
7	+22°, −64°
8	+63°, −22°
	Experimental $\delta_{\min}$ ±(51°–54°)[b]

[a]For the purpose of calculation, the coordinates of sites 5–8 were chosen as follows: sites 6 and 7 lie on the twofold axes of the first- and second-layer atoms and sites 5 and 8 lie in the threefold sites formed by first- and second-layer atoms. All of these sites were placed at a distance of 1.1 Å from the $[1\bar{1}\bar{1}]$ rows for reasons to be shown in Sec. IV B.

[b]From data of Figs. 10 and 11. These are the minima corresponding to W shadowing O. The other minima at 0° (Figs. 10 and 11) and ±90° (some α values of Fig. 11) are due to O self-shadowing, as shown in Sec. V.

low $\alpha^2_{c,sh}$ at $\delta=0°$. Oxygen in this site would be so high above the first-layer rows that little azimuthal dependence of $I(R)$ and $\alpha_{c,sh}$ would be expected. However, if there were azimuthal dependence, Table I predicts strong W shadowing O minima at $\delta=0°$, $\pm31°$, and $\pm90°$, contrary to the behavior of $I(R)$ in Figs. 10 and 11.

Bridging row site (2). Occupancy of these sites can clearly be eliminated for the same reasons as site (1) above, with the exception of interference with BS along $\delta=0°$; along this azimuth, BS would not be affected by occupancy of site (2) since the O atoms would be away from the trajectories of the $p\approx0$ Ar^+/W collisions. Table I predicts strong $I(R)$ minima near $\delta=\pm17°$ for occupancy of this site, in disagreement with Figs. 10 and 11.

On-top and bridging trough sites (3 and 4). These positions would interfere with BS along $\delta=\pm90°$, for along these azimuths the $\alpha^1_{c,sh}$ value (Fig. 5) in the BS versus α plots results from both first- and second-layer atom collisions. Since these sites do not have a plane of symmetry with the first-layer atoms (which largely define the recoil anisotropy) along the $\delta=0°$ direction, they are inconsistent with the symmetry about this azimuth as demonstrated in the RSCM, RSP and plots of δ dependence (Figs. 10–13). The calculated δ_{min} positions in Table I disagree with the minima of Figs. 10 and 11.

Threefold trough sites (5). These sites, which lie symmetrically between two first-layer W atoms along the $[01\bar{1}]$ azimuth and within the $[1\,\bar{1}\,\bar{1}]$ troughs, are the *only* sites that are consistent with *all* of the experimental data. First, these O atom positions do not interfere with direct $p\approx0$ Ar^+/W collisions along $\delta=0°$ and $\pm90°$, hence the reason for the insensitivity of the first I(BS) versus α peaks and the corresponding $\alpha^1_{c,sh}$ values (Fig. 5 and the SSCM) to oxygen coverage along these azimuths. Second, these sites have a plane of symmetry with the first-layer atoms along the $[01\bar{1}]$ azimuth, consistent with the symmetry about $\delta=0°$ in Figs. 10–13. Third, along the $[1\,\bar{1}\,\bar{1}]$ troughs, O atoms in site (5) are not blocked by W atoms and the interatomic distance between them at full coverage is 2.74 Å, consistent with the I(DR) maxima and $\alpha^2_{c,sh}$ values at $\delta=\pm90°$ in Fig. 10. Fourth, O atoms in site (5) are also not blocked by W atoms along $\delta=0°$. The interatomic oxygen distance at full coverage is short along this azimuth, resulting in shadowing and blocking of O atoms by neighboring O atoms and, consequently, the minimum in I(DR) and maximum in $\alpha^2_{c,sh}$ of Fig. 10 for $\delta=0°$. Fifth, site (5) is consistent with the mimima observed in Figs. 10 and 11 and calculated in Table I in the region $\delta=\pm(51°-54°)$; these δ define alignment of first-layer W atoms with O atoms inside the troughs.

Asymmetrical trough sites (6, 7, and 8). These sites do not have a plane of symmetry with the $[01\bar{1}]$ azimuth and are therefore inconsistent with the symmetry about $\delta=0°$ in Figs. 10–13. The calculated δ_{min} values of Table I do not agree with the symmetric minima observed experimentally.

B. Determination of $[01\bar{1}]$ coordinate of site (5) relative to $[1\,\bar{1}\,\bar{1}]$ rows

1. *Determined from I(R) versus δ scans*

The $[01\bar{1}]$ coordinate x of O atoms in site (5) relative to the $[1\,\bar{1}\,\bar{1}]$ rows can be determined from the $I(R)$ versus δ scans of Fig. 11. Well-defined minima in $I(R)$ versus δ are exhibited for $\alpha=26°$, 33°, and 38° at $\delta_{min}=\pm(49°-54°)$ in these plots. These minima correspond to azimuths along which the O and W atoms are aligned, for in these cases the O atom is strongly shadowed by the neighboring W atom. Since δ_{min} is measured relative to the $[01\bar{1}]$ azimuth, the horizontal distance x of the O atom from

TABLE II. Coordinates determined for the oxygen-adsorption-site position [site (5) in Fig. 1].

	$[01\bar{1}]$ coordinate x relative to $[1\,\bar{1}\,\bar{1}]$ rows		
	α	δ_{min}	x
From I(DR) vs δ scans (Sec. IV B 1)	26°	+50°	1.15 Å
	26°	−50°	1.15 Å
	33°	+54°	1.00 Å
	33°	−54°	1.00 Å
	38°	+50°	1.15 Å
	38°	−49°	1.19 Å
		$\langle x\rangle=1.11$ Å, $\sigma=0.08$ Å	
From $\alpha^2_{c,sh}$ vs δ scans (Sec. IV B 2)		±51°	1.1 Å
		$x=1.1\pm0.1$ Å	

	[211] coordinate z relative to plane of first-layer atoms	
	Projectile	z
From p and $R(L)$ vs L (Sec. IV C 1)	4-keV Ar^+	0.50 Å
	5-keV Ne^+	0.55 Å
	$\langle z\rangle=0.5\pm0.1$ Å	
From position of SR peak (Sec. IV C 2)	$z=0.44\pm0.1$ Å	

the $[1\,\bar{1}\,\bar{1}]$ rows for site (5) is $x=(\frac{2.74}{2})/\tan\delta_{\min}$ (Å). The results, shown in Table II, provide the average value $x=1.11$ Å with standard deviation $\sigma=0.08$ Å.

2. *Determined from $\alpha^2_{c,\mathrm{sh}}$ versus δ scans*

The x coordinate can be determined from the $\alpha^2_{c,\mathrm{sh}}$ versus δ plot of Fig. 10, the RSCM, and the RSP. Symmetrical maxima are observed in Fig. 10 at $\delta=\pm 51°$. These $\alpha^2_{c,\mathrm{sh}}$ values define the δ along which the O and W atoms are aligned for a true DR event. The $\alpha^1_{c,\mathrm{sh}}$ value is not used because it can be effected by SR events which are most prominent for low α values. Considering the uncertainties in δ, the coordinate can be calculated as above, yielding $x=1.10\pm 0.10$ Å.

C. Determination of [211] coordinate of site (5) relative to plane of first-layer W atoms

1. *Determined from impact parameter p and shadow cone*

Since the p for DR of O from Ar and Ne into $\phi=65°$, the shape of the Ar-W and Ne-W shadow cones,[6] and the $[01\bar{1}]$ coordinate x are known, the [211] corrdinate z relative to the first-layer W atoms can be obtained as shown in Fig. 15. The experimental data used for the determination are the $I(R)$ versus α scans along $\delta=51°$ (corresponding to alignment of the neighboring W and O atoms) with both 4-keV Ar^+ and 5-keV Ne^+. These scans, shown in Fig. 15, exhibit well-defined second peaks with $\alpha^2_{c,\mathrm{sh}}=30°$ and 18°. The calculated p for ^{40}Ar and ^{20}Ne recoiling ^{16}O into $\phi=65°$ are 0.355 and 0.200 Å, respectively. The shapes of the shadow cones, i.e., the radius R as a function of the distance L behind the W atom, were obtained from the calibrated shadow-cone calculations of I,[6] using the Biersack-Ziegler (BZ) potential[19] with screening constant $C_{\mathrm{BZ}}=0.99$. The radius of the Ar-W cone is ~ 15–20% larger than that of the Ne-W cone. The coordinate z, i.e., the distance of the O atom above the plane of the first-layer atoms, can be obtained as the sum of the distances $|\overline{TQ}|+|\overline{QO}|$ (see Fig. 15). Here, T is a point below the O atom position in the plane of the first-layer W atoms with coordinates

$$R_T=r\sin\alpha^2_{c,\mathrm{sh}},\quad L_T=r\cos\alpha^2_{c,\mathrm{sh}}\ . \tag{2}$$

Q is the intersection of the calculated R and the normal to the surface passing through T, defined by

$$R=-\tan(\pi/2-\alpha^2_{c,\mathrm{sh}})L+r/\sin\alpha^2_{c,\mathrm{sh}}\ . \tag{3}$$

$|\overline{QO}|$ can be approximated by

$$|\overline{QO}|=p/\cos\alpha^2_{c,\mathrm{sh}} \tag{4}$$

using the experimental $\alpha^2_{c,\mathrm{sh}}$'s and the calculated p's. The results are $z=0.50$ and 0.55 Å for Ar and Ne, respectively, with an uncertainty of ± 0.10 Å. The large circles in Fig. 15 are scaled to the covalent radii of the W and O atoms.

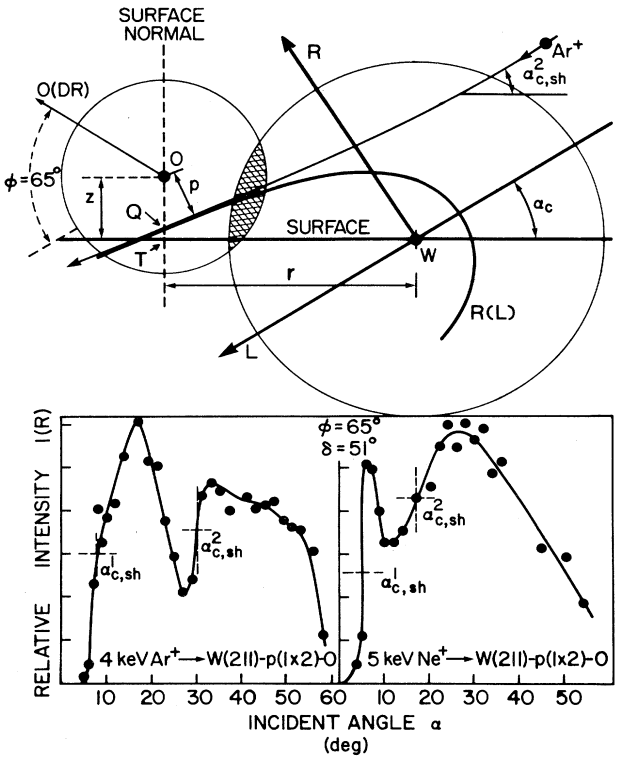

FIG. 15. Lower: $I(R)$ vs α at $\delta=51°$ for 4-keV Ar^+ and 5-keV Ne^+ on the W(211)-$p(1\times 2)$-O surface. The $\alpha^i_{c,\mathrm{sh}}$ values are indicated. Upper: Schematic diagram showing the use of the experimental $\alpha^2_{c,\mathrm{sh}}$'s, the horizontal distance r from a first-layer W atom to site (5) along $\delta=51°$ as determined from the coordinate x in Sec. IV B, and the calculated impact parameter p and shadow cone [$R(L)$ vs L] to determine the vertical coordinate z of the O atom above the plane of the first-layer W atoms. The hatched area denotes the overlap of the W and O covalent radii.

2. *Determined from position of surface recoil peak*

The position of the drifting SR peaks, as shown in Fig. 3, can be used to obtain the [211] coordinate z as follows. Consider an SR trajectory similar to that shown in Fig. 16 in which Ar^+ projectiles are focused at the edge of the W shadow cone and collide with an O atom with p above the center of the O atom. Unlike the case of a single-collision DR event where p is below the center of the O atom and the recoil occurs outward from the surface, in this case the recoil occurs down towards the surface and is sequentially scattered outward from the deeper W layers. Due to the high sensitivity ($\cos^2\phi$ dependence) of the O(DR) energy to ϕ (and p) and the insensitivity of the scattered O energy to θ (due to the large mass disparity of O and W), the final O(SR) energy is determined primarily by the initial DR event, i.e., the initial p. For small α, p is large (but on the opposite side of the O atom from the true DR case), resulting in an O(SR) of approximately the same TOF as a true O(DR), hence the single, broad DR peak observed for $\alpha<9°$ in Fig. 3. As α increases, p decreases, resulting in a more energetic O(SR) atom as seen by the two peaked structures for α near 10°–13° in Fig. 3;

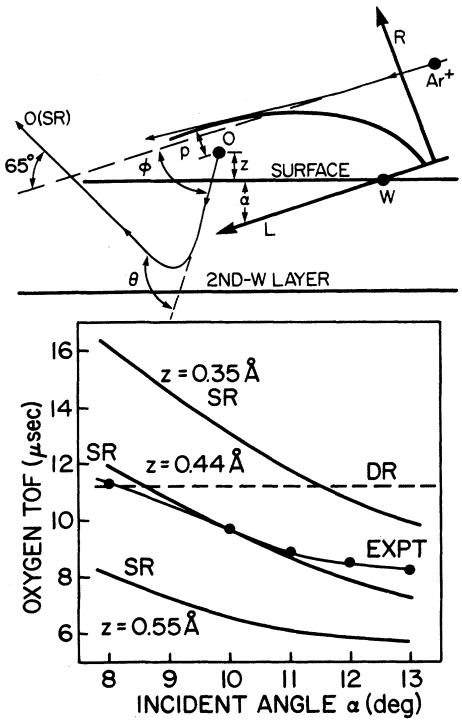

FIG. 16. Upper: Schematic illustration of a surface recoil event in which an Ar^+ projectile recoils an O atom into ϕ and the O atom scatters from the second-layer W atoms into θ. Lower: Calculated TOF vs α for O(SR) into 65° compared to the experimental TOF of the drifting recoil peak at $\delta = 51°$, $\theta = 65°$ in Fig. 3. The three calculated curves assume $x = 1.11$ Å and $z = 0.35$, 0.44, and 0.55 Å.

when $p = 0$, the O(SR) energy is at its highest (lowest TOF). Since the final ejection angle ϕ (position of detector relative to Ar^+ beam) and the shape of the W shadow cone are known, the final energy (and corresponding TOF) of the O(SR) atom can be calculated for different Ar^+ incident angles α and an assumed initial position for the O atom. The site coordinate z was varied in order to obtain the best fit with the experimental TOF. The calculated TOF of the O atom as a function of α for the site coordinates $x = 1.11$ Å, $z = 0.35$, 0.44, and 0.55 Å are shown in Fig. 16 along with the TOF corresponding to a true DR event and the experimental TOF of the drifting SR peak (low TOF recoil peak) from Fig. 3. Due to the strong dependence of the recoil energy on p, changes of 0.1 Å in the assumed value of z result in large (> 2 μsec) variations in the final oxygen TOF. The best fit was obtained for $z = 0.44$ Å, which is in good agreement with the results of Sec. IV C 1. It is assumed, for the purpose of calculation, that the O atom reflects from the deeper layer W atoms in a single scattering collision; reflection by means of a double collision yields a final TOF for which the maximum difference from those shown in Fig. 16 is ~0.5 μsec. The differences between the calculated TOF for $z = 0.44$ Å and the experimental TOF curves are < 1 μsec over the α range for which the drifting peak is observed. This calculation provides a quantitative identification of the drifting peak of Fig. 3, while simultaneously supporting the adsorption site coordinates determined previously.

V. SITE OCCUPANCY VERSUS O_2 DOSE

The occupancy of the threefold trough sites identified in Sec. IV as a function of exposure to O_2 can be determined through use of data such as that of Fig. 14 along with shadowing and blocking trajectory calculations as shown in Fig. 17. Along the $\delta = \pm 90°$ azimuths, $\alpha_{c,\mathrm{sh}}$ is determined by O atoms shadowing O atoms and $\alpha_{c,\mathrm{bl}}$ is determined by O atoms blocking O atoms as follows. Consider the high coverage $p(1\times2)$-O structure corresponding to $\alpha_{c,\mathrm{sh}} = 24°$ and $\alpha_{c,\mathrm{bl}} = 42°$ of Fig. 14. The simulation of Fig. 17 shows Ar^+ approaching ($\alpha = 24°$) a row of oxygen atoms (spacing of 2.74 Å) and the resulting Ar scattering (top frame) and O(DR) (bottom frame) trajectories. Shadow cones are formed behind the O atoms; since Ar is heavier than O, small-p collisions result in penetration of some Ar trajectories into the O cones. Note that the O atoms strongly focus the Ar trajectories such that they are concentrated between the O atoms (top frame). The O(DR) trajectories are strongly blocked by neighboring O atoms (bottom frame); these O trajectories are focused at an angle ($\beta \sim 42°$) considerably higher than the edge of the blocking cone ($\beta \sim 23°$). Focusing of O(DR) trajectories at this high β angle is a result of the concentration of Ar trajectories between the O atoms. The perpendicular distance from the original position of the O(DR) atom to the edge of the highly focused Ar flux

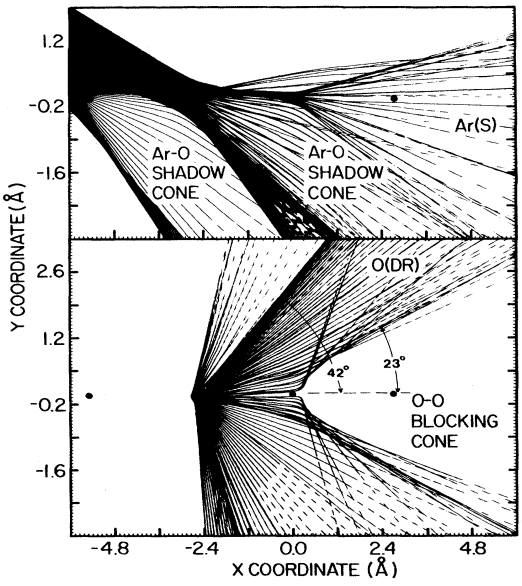

FIG. 17. Upper: Scattering trajectories for 4-keV Ar^+ incident from the left side at $\alpha = 24°$ on a row of oxygen atoms with internuclear spacing of 2.74 Å. Lower: oxygen DR trajectories resulting from the above Ar collisions. The initial positions of the O atoms before collision are shown. Note the different scales on the ordinate and abscissa.

that is concentrated between O atoms is ~ 0.36 Å, i.e, the approximate p required for DR at $\phi = 65°$. In the $I(R)$ versus α scans of Fig. 14, when α increases to the level that $p = 0.36$ Å for the Ar/O collision, the O(DR) flux is focused at $\phi = 65°$ and a sharp rise in I(DR) occurs, defining $\alpha_{c,\mathrm{sh}}$. This corresponds to $\alpha_{c,\mathrm{sh}} = \phi - \beta$, where $\beta = 42°$ as in Fig. 17. Since we are using a fixed $\phi = 65°$, as α increases, β decreases until at $\beta \sim 23°$ the focused O(DR) flux is at the edge of the blocking cone, and I(DR) drops sharply, defining $\alpha_{c,\mathrm{bl}}$ and β_c. The $\alpha_{c,\mathrm{sh}}$ and $\alpha_{c,\mathrm{bl}}$ values for the $p(1\times 2)$-O structure of Fig. 14 are therefore in agreement with the simulations for O-O interatomic distances of 2.74 Å along the $\delta = \pm 90°$ azimuths corresponding to occupancy of every adjacent site.

Consider the low coverage $p(2\times 1)$-O structure corresponding to $\alpha_{c,\mathrm{sh}} = 16°$ and $\alpha_{c,\mathrm{bl}} = 48°$ of Fig. 14. For Ar incident at $\alpha = 16°$, the edge of the highly downward focused Ar flux is at $p = 0.36$ Å for O(DR) into $\phi = 65°$ when the O-O interatomic distance is near 5.5 Å. This spacing also yields focusing at the edge of the blocking cone for $\alpha = 48°$. The $\alpha_{c,\mathrm{sh}}$ and $\alpha_{c,\mathrm{bl}}$ values for the $p(2\times 1)$-O structure are therefore in agreement with the simulations for O-O interatomic distances corresponding to occupancy of every other site along the $\delta = \pm 90°$ azimuths.

The possibility of occupancy of only every third or more site along the $\delta = \pm 90°$ azimuths for the $p(2\times 1)$-O structure was tested by the above method. For occupancy of every third site, the edge of the downward focused Ar flux is ~ 0.7 Å from the O atom and cannot cause focusing of the O(DR) flux at $\phi = 65°$. Larger distances between O atoms provide even poorer agreement with experiment.

For the $\delta = 0°$, azimuth, the O-O interatomic distance is only ~ 2.3 Å if both sides of the troughs are filled, making the blocking effect significantly stronger than along the $\delta = \pm 90°$ azimuths. This is the reason for the low $I(R)$ along the $\delta = 0°$ azimuth in Figs. 9–11. Since only every other trough has all of the sites occupied (see Sec. VI), there are both short and long O-O interatomic spacings along the $\delta = 0°$ azimuth. For the other azimuths, O(R) is shadowed and blocked mainly by W atoms rather than O atoms. For example, in Fig. 14 for the $[11\bar{3}]$ azimuth, the $p(1\times 2)$-O structure has two peaks. The first peak or $\alpha^1_{c,\mathrm{sh}}$ results from both SR and DR of O atoms that are on both the near and far sides, respectively, of the troughs with respect to the beam direction. The second peak or $\alpha^2_{c,\mathrm{sh}}$ results from DR of O atoms on the near side of the troughs.

Preliminary data acquired for the low-dose $p(2\times 1)$-O structure are consistent with occupancy of site (5) in Fig. 1, albeit with different site coordinates. The $[01\bar{1}]$ coordinate appears to be shorter at low dose, i.e., the O atom is closer to the $[1\bar{1}\bar{1}]$ rows than for the saturation $p(1\times 2)$-O case.

VI. DISCUSSION

The results show that O_2 is dissociatively adsorbed in the threefold sites formed by the first- and second-W layers [site (5) in Fig. 1] from low coverages up to more than $\Theta = 1.5$ ML. The data are not consistent with molecular chemisorption. Dissociative chemisorption at site (5) is in agreement with the predictions of Benziger and Preston[11] (B&P) from LEED results. The LEED and TOF-SARS data complement each other. Whereas LEED is capable of directly determining the adsorbate site symmetry pattern and coverage, TOF-SARS is capable of directly measuring the adsorbate-substrate and adsorbate-adsorbate interatomic spacings.

B&P have suggested that the $p(1\times 2)$ surface consists of alternating slightly expanded and contracted troughs commensurate with filling of both sides and only one side, respectively, of the troughs. Our results did not show evidence for such an adsorbate-induced reconstruction, although if the expansion and contraction is small (e.g., $< 5\%$), the measured $\alpha^1_{c,\mathrm{sh}}$ value for $\delta = 0°$ would be an average value for the expanded and contracted troughs which may not be different from the case of symmetrical troughs. However, the shift of the BS peaks to 3°–4° higher α values upon O_2 chemisorption (Sec. III B 2 and Fig. 8) is precisely the amount expected if the relaxed W(211) surface reverts to a bulk-truncated surface. The vertical spacing between the first- and second-atomic layers of the clean W(211) surface was found in I (Ref. 6) to be contracted by 0.12 ± 0.07 A (9.3%). Our results are thus compatible with O_2-induced removal of this relaxation such that the surface layers have interatomic spacings that are close to the bulk spacings. We cannot determine the precise value of the first- to second-layer spacing because the relaxed structure is determined from $\alpha^2_{c,\mathrm{sh}}$ changes of only 3°–4° in BS along specific azimuths, while the presence of O atoms deflects the Ar^+ and Ne^+ BS trajectories by several degrees along these same azimuths. The fact that the 3°–4° increase in $\alpha^2_{c,\mathrm{sh}}$ upon O_2 chemisorption is observed along *all* azimuths rather than only those where the BS trajectories can be deflected by O atoms is direct evidence that the surface has reverted to the bulk-truncated structure.

Three-dimensional trajectory simulations[20] have the requisite sensitivity to distinguish between these two phenomena. Note that this interference is specific to this system and is not a general limitation. For systems in which the adsorbate atoms do not interfere with ion trajectories along the azimuths used to determine relaxation or reconstruction, adsorbate-induced surface structural alterations will be detectable. It can be concluded, however, from the similarities of the SSCM and SSP of the clean and oxygen-covered surface and the small increase in $\alpha^2_{c,\mathrm{sh}}$ upon chemisorption, that the presence of oxygen adsorbates causes no major reconstruction (such as removal of alternating W $[1\bar{1}\bar{1}]$ rows) although it appears to shift the W-W interatomic spacings closer to the bulk values.

A schematic view of O atoms in the threefold sites of the W(211) surface along the $[1\bar{1}\bar{1}]$, $[01\bar{1}]$, and [211] azimuths using the coordinates determined in Sec. IV is shown in Fig. 18. It is observed that despite the fact that the centers of the O atoms are 0.5 Å above the centers of the first-layer W atoms, the tops of the O atoms are lower than the tops of the first-layer W atoms due to the relatively small oxygen radii. Therefore, even at full oxygen

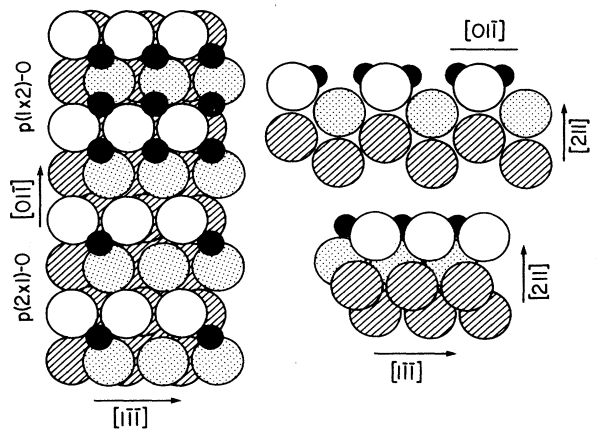

FIG. 18. Views of the W(211)-$p(1\times2)$-O structure along the [211], [01$\bar{1}$], and [1 $\bar{1}$ $\bar{1}$] azimuths using the O atom coordinates determined herein. The sizes of the atoms are scaled according to the covalent radii.

coverage, the first-layer W atoms are still directly exposed to the vacuum. Using the coordinates found for site (5), the interatomic distance from the O atom to the two first-layer W atoms is 1.83 Å and to the second-layer W atom is 2.17 Å for the unrelaxed (bulk-truncated) structure. The difference in these bond lengths is in keeping with the unsaturated and fully saturated valencies of the first- and second-layer W atoms, respectively. Since the measurement is made with respect to the first-W layer, the first-layer W—O bond length is independent of relaxation. For the second-layer W—O bond length, we accept the unrelaxed value based on the above discussion rather than the 2.05-Å value obtained for the relaxed structure. The overlap of the covalent radii of the O atom and a first-layer W atom along their axis is shown in Fig. 15. At full coverage, the first-layer W atoms are coordinated to as many as four O atoms in this manner. Such coordination weakens first- and second-layer W—W atom bonding and facilitates desorption of metal-oxide species for the full $p(1\times2)$-O structure.

These threefold sites are equivalent to the sites for oxygen adsorption on W(110) as determined by LEED (Ref. 21) and electron-stimulated desorption[22] measurements, with the exception that on the W(211) surface, two members of the threefold sites are in the first-W layer and the other member is in the second-W layer. On the W(110) surface all three W atoms of the site are equivalent and in the first-layer. The oxygen-tungsten chemisorption bond length to these three W atoms determined for these sites on the W(110) surface is 2.08 Å from LEED results,[21] 2.02 Å from the bond-order–bond-length relationship,[23] and 1.95 Å from Slater's radii.[24] On the W(211) surface the oxygen-tungsten chemisorption bond lengths determined herein are shorter to first-layer W atoms and longer to second-layer W atoms when compared with the above values. This reflects the low coordination of the first-layer W atoms and their unfulfilled valency (oxygen chemisorption satisfies these deficiencies) and the completely saturated valency of the second-layer W atoms.

The adsorbate site position was determined herein directly from the experimental data and simple calculations performed on laboratory minicomputers. The horizontal and vertical site coordinates were each obtained from different types of experimental measurements; the good agreement between the result from the different measurements lends confidence in the coordinates determined. The calculations employed are only two-dimensional simulations which are not capable of representing some of the three-dimensional interactions that occur. A program is being developed[20] for such interactions.

Adsorption of O_2 on the W(211) surface has provided an excellent test case for the adsorbate structural capabilities of TOF-SARS. The combination of both BS and recoiling provides direct determination of the adsorbate-site symmetry and coordinates. The site symmetry is represented by the scattering and recoiling structural contour maps and plots and the coordinates are determined from the critical incident angles $\alpha^i_{c,\mathrm{sh}}$ for O(R). The use of recoiling[3–5] extends the capabilities of the ion-scattering technique to structural analysis of light adsorbates. The demonstrated sensitivity of the technique to details of the adsorbate-substrate registry, ability to directly determine adsorption-site coordinates, excellent reproducibility and precision with which the measurements can be made, and simplicity of the interpretations suggest that TOF-SARS has tremendous potential as an adsorbate crystallographic technique. It is complementary to LEED since it allows unambiguous distinction between adsorption-site models which, in many cases, cannot be differentiated by LEED patterns alone. The open structure of the W(211) surface provides for at least eight geometrically different adsorption sites, rendering the O/W(211) system substantially more difficult to study than most surfaces. The successful location of the adsorption sites for this system indicates that TOF-SARS will be applicable to many other systems.

The present limitations of TOF-SARS for determining adsorbate structures on surfaces are as follows.

(i) The technique is rather slow. A single I(BS) or $I(R)$ versus α scan can be made in $\sim$15 min, although collection of an entire SSCM or RSCM including reannealing time requires about 20–25 h. Individual scans along certain azimuths may be sufficient for many structural determination cases.

(ii) The limited resolution of TOF analysis precludes separation of DR peaks from heavy adsorbates of similar masses.

(iii) It is sometimes difficult to separate direct from surface recoils, resulting in uncertainties in the collision impact parameter p.

(iv) The existence of adsorbate domains with differing orientations can complicate the results.

VII. CONCLUSIONS

The specific results of this study can be serialized as follows.

(i) The demonstrated high sensitivity of the TOF-SARS technique to light adsorbates such as oxygen, rendered by TOF analysis of both BS and recoil neutrals and ions, allows determination of adsorbate symmetry and site coordinates on surfaces in three dimensions to an accuracy of <0.1 Å.

(ii) The features of the scattering structural contour maps and scattering structural plots are determined by BS from W. By comparison to the SSCM and SSP of clean W(211), these maps reveal that there is no reconstruction of the basic symmetry of the surface upon O_2 chemisorption. However, the increase in the $\alpha^i_{c,\mathrm{sh}}$ values upon O_2 chemisorption indicates that the relaxed W-W interatomic spacings of the clean surface revert to spacings close to the bulk values upon chemisorption. The features of the recoiling structural contour maps and recoiling structural plots are determined by the adsorbate-site positions; these site positions are found to be symmetrical about the $[01\bar{1}]$ $\delta=0°$ azimuth.

(iii) Adsorption of O_2 on the W(211) surface has been characterized as dissociative chemisorption at threefold trough sites formed by two first-layer atoms and one second-layer atom. The values determined for the site coordinates relative to the W lattice for the saturation coverage $p(1\times2)$ structure are as follows: $[1\bar{1}\bar{1}]$ coordinate—symmetrically bridging between two first-layer atoms and lying on the $[01\bar{1}]$ axis; $[01\bar{1}]$ coordinate—1.10 ± 0.10 Å from the close-packed W $[1\bar{1}\bar{1}]$ rows; [211] coordinate—0.50 ± 0.10 Å above the plane of the first-layer W atoms. The oxygen-tungsten chemisorption bond length is determined as 1.83 Å to first-layer W atoms and 2.17 Å to second-layer W atoms. The same symmetry sites are also occupied for the low-dose $p(2\times1)$ structure, although the site coordinates differ; the O atoms appear to be closed to the $[1\bar{1}\bar{1}]$ rows in this structure.

(iv) The degree of occupancy of the adsorption sites can be monitored by the combination of TOF-SARS and LEED. At low exposure [$p(2\times1)$-O structure] every other site along the $[1\bar{1}\bar{1}]$ direction is occupied for a coverage of 4×10^{14} atoms/cm^2. At high exposure [$p(1\times2)$-O structure] every site is occupied along the $[1\bar{1}\bar{1}]$ direction on both sides of the trough for every other trough for a coverage of 1.2×10^{15} atoms/cm^2.

(v) Simple shadowing- and blocking-cone and trajectory-simulation calculations performed on laboratory minicomputers and calibrated to known interatomic spacings are adequate for interpretation of many of the observed BS, FS, DR, and SR features and for determination of adsorbate-site coordinates.

ACKNOWLEDGMENTS

The authors are grateful to R. R. Rye (Sandia Laboratories, Albuquerque, NM) for providing the W(211) crystal and for many helpful discussions. We appreciate the help of Y. Lifshitz, F. Masson, and R. R. Rye for critically reading the manuscript. This material is based on work supported by the National Science Foundation under Grant No. CHE-88-14337 and the Texas Advanced Research Program.

*Permanent address: Universidad Nacional del Comahue, Centro Regional Bariloche, 8400 San Carlos de Bariloche, Argentina.

[1]D. P. Woodruff and T. A. Delchar, *Modern Techniques of Surface Science* (Cambridge University Press, Cambridge, 1986).
[2]Th. Fauster, Vacuum **38**, 129 (1988).
[3]J. W. Rabalais, CRC Crit. Rev. Solid State Mater. Sci. **14**, 319 (1988).
[4]B. Visscher, Ph.D. Dissertation, Rijksuniversiteit, Groningen, The Netherlands, 1988.
[5]B. J. J. Koeleman, S. T. deZwart, A. L. Boers, B. Polsema, and L. K. Verheij, Phys. Rev. Lett. **56**, 1152 (1986).
[6]O. Grizzi, M. Shi, H. Bu, P. Hochmann, and J. W. Rabalais, this issue, paper I, Phys. Rev. B **40**, 10 127 (1989).
[7]M. Shi, O. Grizzi, H. Bu, J. W. Rabalais, and R. R. Rye, this issue, paper III, Phys. Rev. B **40**, 10 163 (1989).
[8]C. C. Chang and L. H. Germer, Surf. Sci. **8**, 115 (1967).
[9]J. C. Tracy and J. M. Blakely, Surf. Sci. **15**, 257 (1969).
[10]Hopkins and G. D. Watts, Surf. Sci. **44**, 237 (1974).
[11]J. B. Benziger and R. E. Preston, Surf. Sci. **151**, 183 (1985).
[12]G.-C. Wang and T.-M. Lu, Phys. Rev. B **31**, 5918 (1985); **28**, 6795 (1983).
[13]J. M. Pimbley and T.-M. Lu, Surf. Sci. **159**, L467 (1985).
[14]G.-C. Wang, J. M. Pimbley, and T.-M. Lu, Phys. Rev. B **31**, 1950 (1985).
[15]J. M. Pimbley, T.-M. Lu, and G.-C. Wang, J. Vac. Sci. Technol. A **4**, 1357 (1986).
[16]J. F. Wendelken, J. Vac. Sci. Technol. A **6**, 662 (1988).
[17]W. P. Ellis and R. Bastasz, in *The Structure of Surfaces II*, edited by J. F. Van der Veen and M. A. Van Hove (Springer, Berlin, 1988).
[18]O. Grizzi, M. Shi, H. Bu, and J. W. Rabalais, Rev. Sci. Instrum. (to be published).
[19]F. Zeigler, J. P. Biersack, and U. Littmark, *The Stopping and Range of Ions in Solids* (Pergamon, New York, 1985).
[20]P. Hochmann, M. Kilburn, M. Shi, and J. W. Rabalais (unpublished).
[21]M. A. Van Hove and S. Y. Tong, Phys. Rev. Lett. **35**, 1092 (1975).
[22]T. E. Madey, Surf. Sci. **94**, 483 (1980).
[23]K. A. R. Mitchell, Surf. Sci. **149**, 93 (1985).
[24]J. C. Slater, *Symmetry and Energy Bands in Crystals* (McGraw-Hill, New York, 1965).